Kim *et al. Soft Sci* 2023;3:18
**DOI:** 10.20517/ss.2023.08

**Soft Science**

**Research Article**

**Open Access**

Check for updates

# Injectable and tissue-conformable conductive hydrogel for MRI-compatible brain-interfacing electrodes

**Sung Dong Kim[1,2,#], Kyuha Park[2,3,#], Sungjun Lee[2,3,#], Jeungeun Kum[4,5], Yewon Kim[2,3], Soojung An[2,3], Hyungmin Kim[4,5], Mikyung Shin[1,2,6,*], Donghee Son[2,3,7,*]**

[1]Department of Biomedical Engineering, Sungkyunkwan University (SKKU), Suwon 16419, Republic of Korea.
[2]Center for Neuroscience Imaging Research, Institute for Basic Science (IBS), Suwon 16419, Republic of Korea.
[3]Department of Electrical and Computer Engineering, Sungkyunkwan University (SKKU), Suwon 16419, Republic of Korea.
[4]Bionics Research Center, Biomedical Research Division, Korea Institute of Science and Technology, Seoul 02792, Republic of Korea.
[5]Division of Bio-Medical Science & Technology, KIST School, University of Science and Technology, Seoul 02792, Republic of Korea.
[6]Department of Intelligent Precision Healthcare Convergence, Sungkyunkwan University (SKKU), Suwon 16419, Republic of Korea.
[7]Department of Superintelligence Engineering, Sungkyunkwan University (SKKU), Suwon 16419, Republic of Korea.
[#]Authors contributed equally.

[*]**Correspondence to:** Prof. Mikyung Shin, Center for Neuroscience Imaging Research, Institute for Basic Science (IBS); Department of Intelligent Precision Healthcare Convergence, Sungkyunkwan University (SKKU); Department of Biomedical Engineering, SKKU, 2066 Seobu-ro, Jangan-gu, Suwon-si 16419, Gyeonggi-province, South Korea. E-mail: mikyungshin@g.skku.edu; Prof. Donghee Son, Center for Neuroscience Imaging Research, Institute for Basic Science (IBS); Department of Electrical and Computer Engineering, Sungkyunkwan University (SKKU); Department of Superintelligence Engineering, SKKU, 2066 Seobu-ro, Jangan-gu, Suwon-si 16419, Gyeonggi-province, South Korea. E-mail: daniel3600@g.skku.edu

**How to cite this article:** Kim SD, Park K, Lee S, Kum J, Kim Y, An S, Kim H, Shin M, Son D. Injectable and tissue-conformable conductive hydrogel for MRI-compatible brain-interfacing electrodes. *Soft Sci* 2023;3:18. https://dx.doi.org/10.20517/ss.2023.08

**Received:** 21 Feb 2023 **First Decision:** 7 Apr 2023 **Revised:** 9 May 2023 **Accepted:** 10 May 2023 **Published:** 25 May 2023

**Academic Editor:** Yihui Zhang **Copy Editor:** Dong-Li Li **Production Editor:** Dong-Li Li

## Abstract

The development of flexible and stretchable materials has led to advances in implantable bio-integrated electronic devices that can sense physiological signals or deliver electrical stimulation to various organs in the human body. Such devices are particularly useful for neural interfacing systems that monitor neurodegenerative diseases such as Parkinson's disease or epilepsy in real time. However, coupling current brain-interfacing devices with magnetic resonance imaging (MRI) remains a practical challenge due to resonance frequency variations from inorganic

metal-based devices. Thus, organic conductive materials, such as poly(3,4-ethylenedioxythiophene)-poly(styrenesulfonate) (PEDOT:PSS), have recently been considered as promising candidates. Nonetheless, their conformability on curvilinear tissues remains questionable. In this study, we developed an injectable conductive hydrogel (ICH) composed of tyramine-conjugated hyaluronic acid (HATYR) and PEDOT:PSS for MRI-compatible brain-interfacing electrodes. Our ICH produced low impedance around 5 kΩ even under 10 Hz, demonstrating high confidence volumetric capacitance. Due to HATYR's biocompatibility, histological and cytotoxicity assays showed almost no inflammation and toxicity, respectively; in addition, ICH was able to degrade into 40% of its original volume within four weeks *in vivo*. An electrocorticogram (ECoG) array was also patternable by syringe injections of ICH on a stretchable and flexible elastomeric substrate layer that conformed to curvy brain tissues and successfully recorded ECoG signals under light stimulation. Furthermore, MRI imaging of implanted devices did not show any artifacts, indicating the potential of the MRI-compatible hydrogel electrodes for advanced ECoG arrays. This study provides a promising solution for MRI-compatible neural electrodes, enabling the advancement of chronic neural interfacing systems for monitoring neurodegenerative diseases.

**Keywords:** Injectable conducting hydrogel, hyaluronic acid, PEDOT:PSS, electrode array, electrocorticogram, MRI

## INTRODUCTION

The development of flexible and stretchable functional materials has enabled advances in both wearable and implantable bio-integrated electronic devices[1,2], which are capable of either sensing physiological/physical signals generated from various organs[3-8] or delivering the electrical/optical stimulations to the desired tissue location in the human body[9-12]. The inherent advantages of such bidirectional and deformable bioelectronic devices have gained considerable interest in chronic neural interfacing systems for the precise monitoring of intractable neurodegenerative diseases, such as multiple sclerosis, Parkinson's disease, Alzheimer's disease, and epilepsy[13]. As a representative example, a flexible thin electrode array coated with biodegradable silk fibroin was conformally mounted onto the brain tissue surface and showed high-performance electrocorticogram (ECoG) sensing capability with high areal uniformity[14]. Although the cortex-conformable interfacing approach has improved our understanding of specific brain activities, to further enable the search of neuronal circuits in the central nervous system (CNS), the information gathered using brain-interfacing devices should be coupled with those of magnetic resonance imaging (MRI)[15]. In this regard, the current utilization of inorganic bio-inert metallic thin films (e.g., Au and Pt) formed by harnessing conventional deposition processes remains a practical challenge.

Organic flexible conductive materials, such as poly(3,4-ethylenedioxythiophene)-poly(styrenesulfonate) (PEDOT:PSS)[16-24], carbon nanotubes[25-28], and graphene[29-31], have been considered promising candidates for MRI-compatible neural electrodes because they do not produce MRI artifacts[32,33]. To achieve better conformability even on the gyri and sulci, a rigid island design strategy employing a strain-dissipative wavy electrode and the mechanically neutral plane has been widely applied to organic conductive materials supported on stretchable substrates[34,35]. Although such an approach has shown remarkable potential in providing a high signal-to-noise ratio (SNR) on a large scale, the areal density remains limited in compensating for the relatively low spatiotemporal resolution of MRI compared to that of the ECoG device, owing to the use of serpentine interconnects[36,37]. Therefore, intrinsically stretchable composites fabricated by the optimal mixing of biocompatible hydrogels with organic conductive fillers have the benefit of reducing cell-to-cell distance efficiently while effectively matching the stiffness of the brain tissue[38,39]. However, there remain limitations associated with patterning issues, where the conducting fillers in the conductive hydrogel composites with photo-crosslinking materials reflect the ultraviolet light used in conventional photolithography, thereby impeding uniform fabrication[40,41]. As an alternative strategy, a syringe-injectable patterning method may facilitate the conventional patterning process while maintaining

both electrical and mechanical characteristics of the organic conductive hydrogel composites[42-44]. Although a few cases of the application of injectable conductive hydrogels (ICHs) to diverse tissues for effective treatment have been reported recently, on-cortex neural sensing with MRI compatibility has not yet been performed[45-49].

In this study, we developed an ICH composed of tyramine-conjugated hyaluronic acid (HATYR) and poly(3,4-ethylenedioxythiophene)-poly(styrenesulfonate) (PEDOT:PSS) for MRI-compatible brain-interfacing electrodes [Figure 1A]. Hyaluronic acid (HA) is a natural polymer abundant in the extracellular matrix of the brain[50]. In particular, chemically modified HA backbones (e.g., functionalization using photocurable methacrylate, norbornene, and other phenolic groups) have been widely used for forming biocompatible hydrogels as 3D bio-printable inks in tissue engineering and drug delivery carriers[45,51-56]. Among them, the tyramine modification of HA can be adopted for the enzymatic crosslinking of polymers, enabling their injectability in a time-dependent manner[57-62]. However, while there are few studies of conductive HA hydrogels[63,64], no study has focused on HATYR to engineer conductive materials for the *in vivo* recording of electrophysiological signals. We hypothesized that the phenol groups (e.g., hydrogen bond donors) in HATYR mediate additional intermolecular interactions with the sulfonyl groups (e.g., hydrogen bond acceptors) of negatively charged PSS via hydrogen bonds, resulting in the reversible ionic crosslinking of the polymers, HATYR and PEDOT:PSS, followed by conductive and injectable gelation as brain-interfacing electrodes. Furthermore, stability both in electrical conductance and against hydrolysis was achieved by the addition of glycerol in the hydrogel to meet the final ICH composition. The fully organic ICH could be *in situ* patternable by syringe injections on a stretchable and flexible poly(vinylidene fluoride-co-hexafluoropropylene) (PVDF-HFP) substrate layer to fabricate an MRI-compatible implantable ECoG multi-channel electrode array on demand. In addition, the ICH-based ECoG array was highly biocompatible and conformally adhered to the soft dura mater, and the T2-weighed MRI did not show any artifacts [Figure 1B]. Furthermore, the array device was capable of successfully recording brain ECoG signals from the visual cortex under light stimulation [Figure 1C], indicating the potential of MRI-compatible hydrogel electrodes for further advanced ECoG arrays.

## EXPERIMENTAL

### Materials

HA at a molecular weight of 700 kDa was purchased from Lifecore Biomedical. Tyramine hydrochloride (TYR) (98%), PEDOT:PSS (high-conductivity grade, 1.1% in $H_2O$), N-hydroxysuccinimide (NHS), and glycerol were purchased from Sigma-Aldrich. Poly(vinylidene fluoride-co-hexafluoropropylene) (PVDF-HFP: "FC-2145") was purchased from 3M Korea. 1-(3-dimethylaminopropyl)-3-ethylcarbodiimide (EDC) hydrochloride (98%) was purchased from Tokyo Chemical Industry.

### Synthesis of HATYR

The conjugation of tyramine moiety onto the HA backbone was performed using EDC/NHS chemistry, as previously reported[65]. First, 1 g of HA was weighed and dissolved at 1% (w/v) in 100 mL of pH 4.7 MES buffer solution (0.1 M) at room temperature. Next, HA equivalent moles of EDC and NHS were added to the mixture and allowed to dissolve for 30 min, after which HA equivalent moles of TYR were added and stirred overnight in a nitrogenous environment. After overnight stirring, the conjugated solution was dialyzed using a 6-8 kDa MWCO membrane in 100 mM NaCl dialysate for two days. After two days, the dialysate was replaced with only deionized distilled water for 4 h, and HATYR was obtained via lyophilization.

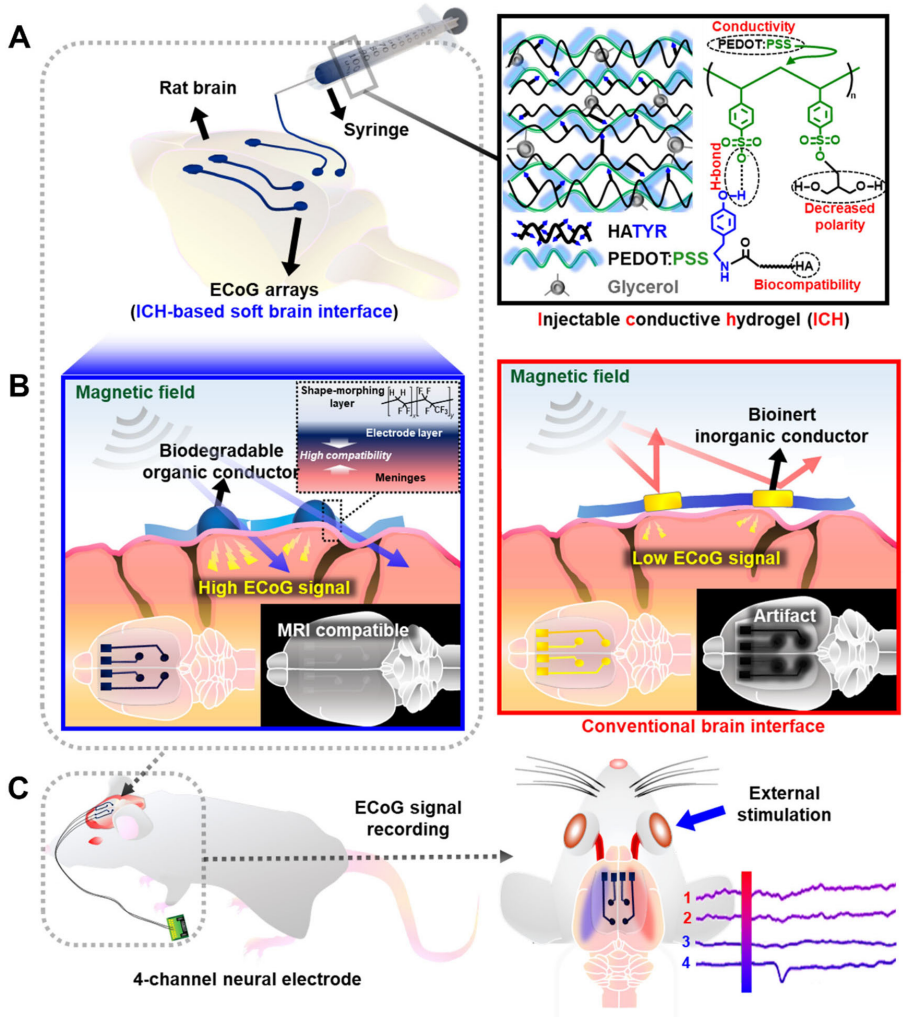


**Figure 1.** The material design of the injectable conductive hydrogel (ICH) for ECoG electrode. (A) Schematic illustration of ICH-based soft brain interface (gray box, left) and ICH structure: HATYR (biocompatible backbone), PEDOT:PSS (conductive segment with green arrow indicating PSS), and glycerol (hydrophobic segment) (black box, right); (B) MRI-imaging scenarios of (i) ICH-based soft brain interface consisting of ICH and conformable substrate (PVDF-HFP) (left blue box) and (ii) ICH-based soft brain interface, which is composed of ICH and conformable substrate (PVDF-HFP) (right red box); (C) Illustration of ECoG signal recording model to ICH-based soft brain interface (left) and principle of ECoG signal recording from left hemisphere from external stimulation (right). ECoG: electrocorticogram; HATYR: tyramine-conjugated hyaluronic acid; PEDOT:PSS: poly(3,4-ethylenedioxythiophene)-poly(styrenesulfonate); PVDF-HFP: poly(vinylidene fluoride-co-hexafluoropropylene).

The lyophilized HATYR was dissolved in $D_2O$ at 1% (w/v), and the degree of tyramine substitution (DOS) of HATYR was measured using $^1$H NMR spectroscopy (Varian Oxford 300 MHz, Palo Alto, CA, USA). The integral value at 6.7-7.1 ppm for four $^1$H present in TYR was compared with that of three $^1$H in the N-acetyl group of the HA backbone at 2 ppm. Then, the DOS of HATYR was further analyzed using an Agilent 8453 UV-Vis spectrometer (Agilent Technologies, Santa Clara, CA, USA). A calibration curve for TYR was initially obtained as $y = 0.0049\ x - 0.0017$ ($x$ = TYR concentration, $y$ = absorbance at 275 nm). The absorbance ($A_{275}$) of the HATYR solutions at different concentrations was evaluated using the TYR calibration equation to determine the DOS.

### Design of HATYR/PEDOT:PSS hydrogel and ICH

HATYR/PEDOT:PSS hydrogel was prepared by simply mixing different weights (0.5, 1, 2, and 3 w/v %) of HATYR with 1.1% of PEDOT:PSS solution using a vortex mixer. Then, the ICH was prepared by adding glycerol to the HATYR/PEDOT:PSS hydrogel at a 2:1 molar ratio to the free PSS moles unlinked to the TYR moieties. Immediately after the addition of glycerol, the hydrogel was thoroughly mixed to form the final ICH formulation.

### Physicochemical evaluation of ICH

To investigate the chemical interactions in the prepared hydrogels, freeze-dried HATYR, PEDOT:PSS, HATYR/PEDOT:PSS, and ICH were observed by Fourier transform infrared (FT-IR) spectral analysis (TENSOR27; Bruker, Bremen, Germany) using the KBr method at a wavenumber resolution of 4 $cm^{-1}$ of 32 scans for each spectrum.

Additionally, to examine the morphological changes of the hydrogel, freeze-dried HATYR, PEDOT:PSS, and HATYR/PEDOT:PSS, a field-emission scanning electron microscopy (FE-SEM) (Jeol JSM-IT800, Tokyo, Japan) was used. In addition, the specific intensities of sulfur elements were further evaluated using energy-dispersive X-ray spectroscopy (EDS).

### Rheological measurements

For the rheological examination of all hydrogel samples, a rheometer (Discovery Hybrid Rheometer, TA Instruments, New Castle, DE, USA) was used. At the settings of 1% strain from 0.01 to 10 Hz, a frequency sweep test was performed to determine the storage modulus, loss modulus, and damping factor of the hydrogels, denoted as G', G", and tan δ, respectively. For the measurement of shear viscosity of the hydrogels, an oscillation test in the shear rate range of 0.01 to 100 $s^{-1}$ was performed. The self-healing behavior of ICH was observed in the rheometer at oscillating strains of 0.5% and 1,000% for every 180 s at a 1 Hz oscillation frequency.

### Injectability and printability characterization of ICH

The injectability of the hydrogels prepared with varying concentrations (0.5, 1, 2, and 3 w/v %) of HATYR was observed using a 30 G needle in a 1-mL syringe. Each hydrogel was tested for extrudability and evaluated using the frequency sweep and oscillation test methods of rheological measurements.

The feasibility of 3D printing was observed using ICH. First, four paths of the electrode array with a total area of 11 mm × 7 mm were designed using the Blender software and exported as a .stl file. The file was then sliced in the NewCreatorK software as a .gcode file. Then, a 15-mL syringe filled with the hydrogel formulation was mounted onto a 3D printer (Dr. INVIVO 4D2; Rokit Healthcare, Seoul, Korea) and printed at a printing speed of 1 mm/s.

### Dissolution and conductive properties ICH

The dissolution resistance of ICH due to addition of glycerol was demonstrated by submerging HATYR/PEDOT:PSS and ICH in 1% phosphate buffer solution (PBS) for 30 min. Photographs were taken to qualitatively observe changes in the morphology of the injected hydrogels. Furthermore, normalized resistivity and conductivity calculations of ICH were performed while soaking in a PBS buffer from 0 to 16 h to observe the electrical durability of ICH from dissolution.

Strain-dependent conductivity tests were performed to measure the electrical performance of glycerol using the following previously reported protocol[66]: a piece of Ecoflex™ 00-30 film was attached to the Motorizer X-translation auto-stretching stage (Jaeil Optical System, Incheon, Korea). The stage was preprogrammed to

perform repeated cyclic strain tests (100 times) from 0 to 100%. The sample was injected in lengths of 15 (ø = 3 mm) onto the stretching stage, followed by wiring an end-to-end line with cables to connect to an inductance/capacitance/resistance meter to determine the electrical performance of the stretched hydrogels. The resistance-strain values were obtained and evaluated using Origin software.

### Preparation and characterization of brain surface interface

Next, 1 g of PVDF-HFP was dissolved in 20 mL of acetone and stirred overnight. The dissolved PVDF-HFP was then poured onto a 100 mm × 100 mm square glass coated with low-density polyethylene. The solution was left to dry for 6 h to fabricate a substrate with a thickness of 100 μm. Then, mechanical tests of the prepared films were analyzed using a universal tensile machine (UTM) (Instron 34SC-1; Norwood, MA, USA), as previously reported[67].

A previously designed four-electrode array mold was 3D-printed using Ultimaker S7 (Ultimaker, Utrecht, Netherlands) with acrylonitrile butadiene styrene (ABS) as the printing material. Then, 100-μm thick PVDF-HFP was cut into a cuboid with a length and width of 13 mm × 9 mm, respectively. The printed four-electrode array mold was then gently stamped onto the cut PVDF-HFP film to leave patterns on the substrate. Then, holes at the end of each array were made using a 1-mm biopsy punch. Finally, ICH was injected along the patterned substrate, leaving approximately 200 μm (diameter) of ICH along 7-mm long outer lines and 2-mm long inner lines.

### The electrochemical impedance of the electrode array device

Electrochemical impedance spectroscopy (EIS) was performed by utilizing a potentiostat (SP1, ZIVE Lab Co., Ltd., Seoul, Korea) according to a previously reported method[68]. A saturated calomel electrode was used as the reference, and a Pt plate (RDE0021, AT Frontier Co., Ltd., Anyang, Korea) was used as the counter electrodes. With a reference and counter electrode soaked in PBS, a soft electrode was gently placed on the surface of the solution. The impedance of the devices according to frequency was profiled for a range of 100 kHz to 10 Hz using a 10 $mV_{rms}$ input signal.

### Conformal contact evaluation

To evaluate the characteristic conformal contact ability of our electrode array device, fully dissolved 1 w/v % agarose gel was poured over a brain mold to fabricate brain-like grooves and fissures. The device was then mounted on the agarose brain to observe the conformal contact. The device was then left overnight to observe the degree of conformal contact according to the curves of the agarose brain phantom model.

### *In vitro* cell viability assay

The cell viability assay was performed in accordance with the ISO 10993-5:2009 *in vitro* cytotoxicity evaluation and previously tested procedure. First, a HT22 cell suspension (50,000 cells per well) was seeded in a 24-well plate with 1 mL of Dulbecco's modified Eagle's medium supplemented with 1% sodium pyruvate, 10% fetal bovine serum, and 1% penicillin/streptomycin and preincubated at 37 °C and 5% $CO_2$ for 24 h until 80% confluency was achieved. Then, 100 μL of UV-irradiated ICH and a 20 mm × 20 mm PVDF-HFP film were placed in different respective wells and immersed in 1 mL of the supplemented medium before culturing at 37 °C and 5% $CO_2$ for 24 h. Finally, the cells were washed with Dulbecco's phosphate-buffered saline (DPBS), and a cytotoxicity assay was performed following the staining of live cells with 0.5 mL of calcein AM solution (2 μM) and dead cells with 0.5 mL of ethidium homodimer-1 solution (4 μM). Fluorescent images were obtained using a Leica DMi 8 fluorescent microscope (Leica, Wetzlar, Germany). Using ImageJ, cell viability (%) was calculated as the percentage of the live cells to the total number of cells, including dead cells.

### Acute visual evoked potentialactivation test

The *in vivo* experiment was conducted in 6-week-old Sprague-Dawley rats. The rodents were first anesthetized via an intramuscular injection of a ketamine/xylazine, and the head was fixated on a Model 900 stereotaxic instrument (David Kopf Instrument, Inc., Los Angeles, CA, USA)[69]. The hair and scalp were shaved using a razor blade and incised using operating scissors, respectively. The skull was drilled into an oval shape using an electrical tool (Strong 207s; Saeshin, Inc., Daegu, Korea), followed by removing the trimmed fragment and securing the cortical area.

For the ECoG monitoring from visual evoked potential (VEP), the prepared ICH arrays coupled with a customized adaptor were connected to a Digital Lynx SX neural recording instrument (Neuralynx, Inc., Bozeman, MT, USA). The soft device was conformally mounted onto the epidural surface area, and ICH was injected into the four previously punched channels. Two stainless-steel screws were placed over the frontal lobe as the reference and ground. Prior to VEP activation, baseline ECoG signals were sufficiently accumulated for 5 min. After the baseline signal recordings, the anesthetized rodents were subjected to dark adaptation for 5 min, followed by event-related potential activation from the visual cortex test for 5 min.

The VEP activation test in the left hemisphere is as follows: light stimulation was conducted at 0.2 Hz frequency in the right eye of the rodent using a green LED with the left eye blinded by a black fabric sheet. The documented neural signal data were processed and analyzed using MATLAB.

### *In vivo* degradation of ICH

To evaluate the biodegradation of ICH *in vivo*, 1 mL of ICH was injected onto the surface of the secured left hemisphere of anesthetized rodents. Immediately after the injection, the brain was sealed with the previously cut skull to embed the hydrogel using UV-curable medical glue. The scalp was then sutured, and the rodent was left to recover from sedation.

### Magnetic resonance imaging of the device-implanted rodents

All MRI experiments were performed using a Bruker Biospec 9.4 T/30 cm bore (Bruker, Billerica, MA, USA). The rodents were first sedated with isoflurane, and the head was positioned at the isocenter of the magnet. A birdcage RF coil with an inner diameter of 86 mm was used to produce circular polarization, and a Bruker planar surface coil with an inner diameter of 10 mm was mounted directly on the cradle and positioned above the brain for detection. Magnetic resonance imaging (MRI) measurements were taken in the axial and coronal planes, and the images were processed and evaluated using ImageJ for the qualitative evaluation of the electrode array and the *in vivo* degradation of the ICH.

### Brain extraction and histology

Four weeks after ICH implantation, the rodents were sedated with isoflurane. The completely anesthetized rodents were then cut open below the diaphragm, and the rib cage was cut to expose the heart. A needle mounted on a 50-mL syringe filled with saline solution was inserted into the left ventricle, and a small incision was made in the right atrium. Perfusion was performed by injecting 150 mL of saline solution. The head was then decapitated, and the bones and skin were carefully removed to extract the cerebral cortex. The extracted brains were then fixed in 4% paraformaldehyde for 24 h at room temperature.

Next, the fixed brains were sliced and stained with hematoxylin and eosin (H&E) and Masson's trichrome (MT) staining at Genoss Co., Ltd. (Suwon, South Korea). The stained specimen was imaged using an optical microscope for the evaluation of diseased cells, tissues, and fibrosis.

### Feasibility of ICH in electrocardiogram and electromyogram

Both electrocardiogram (ECG) and electromyogram (EMG) measurements were performed as previously reported[67,70,71]. For the ECG measurement, three sensing and reference electrodes were attached to the left arm, right arm, and left foot, respectively, of a volunteer. Subsequently, the ECG signals were recorded using a bio-signal amplifier (Bio Amp FE231; AD Instruments, Oxford, UK) and a data acquisition device (DAQ) (PowerLab 8/35; AD Instruments, Oxford, UK). The recorded ECG signals were processed using a low-pass filter of 1,500 Hz in accordance with the International Society of Electrophysiology and Kinesiology (ISEK) standards.

For EMG measurements, the three electrodes were attached to the upper arm, elbow, and lower arm, respectively. The EMG signals were recorded from flexion and extension of the forearm at intervals of 3 s using the measurement setup comprising of an amplifier, DAQ, and low-pass filter.

### Statistical analysis

All statistical analyses were performed by analysis of variance using the software Origin, and all of the results are presented as mean ± standard deviation (SD). Differences are defined as ns for "not significant" and significant at $^{*}P < 0.05$, $^{**}P < 0.01$, $^{***}P < 0.001$, and $^{****}P < 0.0001$. Unless stated otherwise, at least three independent tests were performed for each result.

## RESULTS AND DISCUSSION

### Characterization of ICH

Conjugation of tyramine to HA was first conducted to synthesize HATYR. The results of UV-vis [Supplementary Figure 1A] and $^{1}$H-NMR spectroscopy [Supplementary Figure 1B] indicated that the degree of substitution for tyramine to HA was approximately 6.29% ± 0.31% and 7.24% ± 0.14 %, respectively.

For the gelation of HATYR and PEDOT:PSS into a soft hydrogel, the two polymers were mixed together in water. Hydrogel is a highly porous and biocompatible structure with ionic conductivity and tissue-like properties[72]. Particularly, hydrogel-based implantable electrode arrays have their advantages in implantable devices due to their ability to conformally interface with target biological tissues with matching mechanical modulus. Moreover, hydrogels are intrinsically soft and water-rich, therefore allowing for injectability and patternability, along with biocompatibility, when implanted in the body[73,74].

Hydrogen bonds formed between hydroxyl groups in HATYR and the sulfonate group of PSS, with the sulfonate group of PSS mainly acting as a hydrogen bond acceptor to crosslink with the phenol group of tyramine [Figure 2A]. This was first observed in the FT-IR spectrum, where the O-H[75], C-C, and C=C peaks at 3439, 2936, and 2866 $cm^{-1}$, respectively, increased as the concentration of HATYR increased [Figure 2B, left]. In addition, the C=O carboxyl peak at 1,736 $cm^{-1}$ indicates that the HA backbone also participates in ionic crosslinking with PEDOT:PSS. More importantly, the C=O amide shifted from 1,632 $cm^{-1}$ to 1,654 $cm^{-1}$ as the concentration of HATYR increased, indicating that the amide bond between the tyramine and the HA backbone stretched due to hydrogen bonding at the phenol end of tyramine [Figure 2B, right][76].

The chemical difference between HATYR/PEDOT:PSS and ICH, that is, the presence of glycerol, was evaluated in the FT-IR spectrum, and the disappearance of C=C[77] and C-O-C[78] of PEDOT at 1,550 and 1,490 $cm^{-1}$, respectively, was attributed to the broken bonds between PEDOT and PSS due to glycerol. However, $-SO_3^-$[77,79] appeared at 1,296 and 1,180 $cm^{-1}$, which indicated stretching of the sulfonate due to the covalent crosslinking of PSS with glycerol as the sulfonic acid group of PSS and the hydroxyl group of

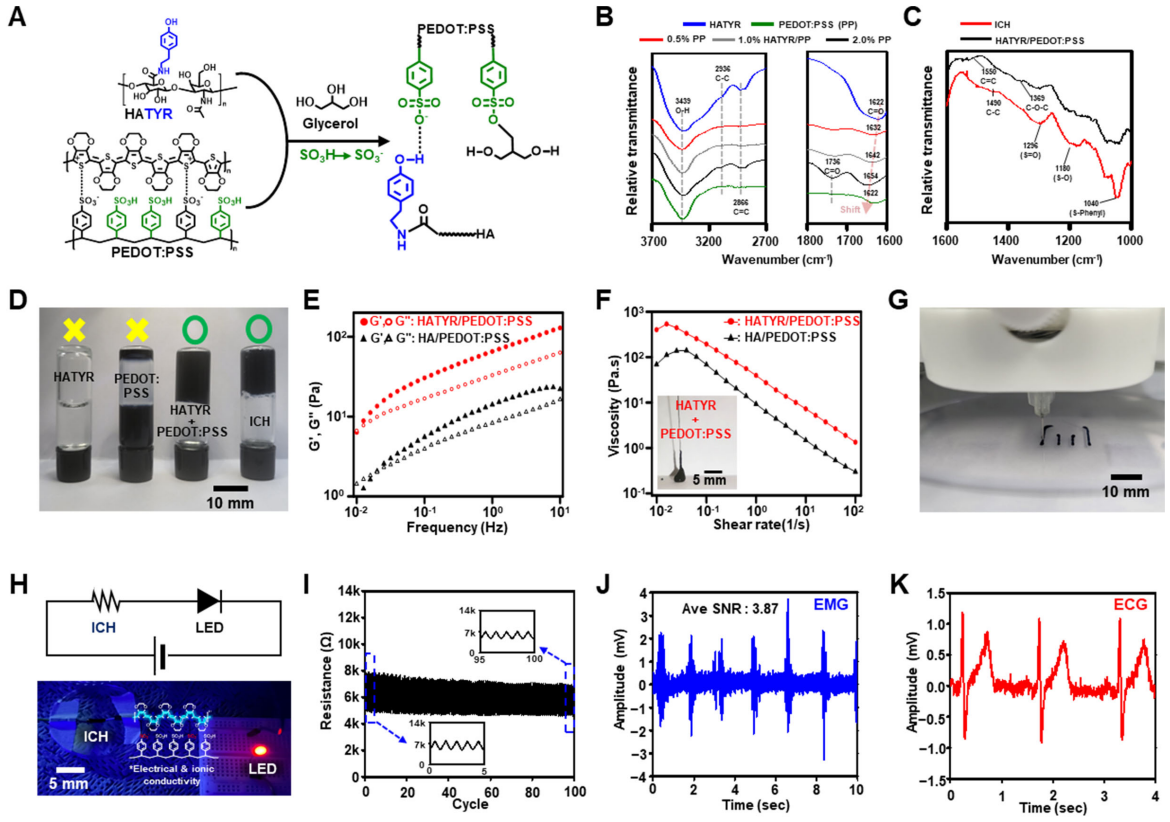


**Figure 2.** Characterization of ICH. (A) ICH chemical interaction mechanism. Tyramine binds to deprotonated sulfonate of PSS by hydrogen bonding, while glycerol covalently binds with deprotonated sulfonate of PSS; (B) FT-IR spectra of HATYR (blue), 0.5% HATYR/PEDOT:PSS (red), 1% HATYR/PEDOT:PSS (gray), 2% HATYR/PEDOT:PSS (black), and PEDOT:PSS (green); (C) FT-IR spectra of HATYR/PEDOT:PSS hydrogel (black) and addition of glycerol (ICH) (red); (D) Photograph of gelation of HATYR/PEDOT:PSS and ICH; (E) Oscillation frequency sweep measurements of HA/PEDOT:PSS (black) and HATYR/PEDOT:PSS (red) hydrogels. The filled circles represent the storage modulus (G'), and the empty circles represent the loss modulus (G"); (F) Viscosity with increasing shear rates (0.01-100 $s^{-1}$) of HA/PEDOT:PSS (black) and HATYR/PEDOT:PSS (red) hydrogels (injectability of HATYR:PEDOT:PSS in 30 G needle, inset photo); (G) 3D printing of electrode array design using ICH; (H) LED demonstration of ICH: photograph (top) and circuit model (bottom); (I) Reversible electrical reliability of the ICH during cyclic stretching/releasing tests (at a speed of 0.3 mm/s and strain of 100%) on one hundred times (inset images represent initial and final 5 peaks); (J) Real-time monitoring of EMG signal from repeated open-clenching, based on ICH-electrode; (K) ECG signals with typical P-Q-R-S-T wave monitoring via ICH-electrode without filtering. ECG: electrocardiogram; EMG: electromyogram; FT-IR: fourier transform infrared; HATYR: tyramine-conjugated hyaluronic acid; ICH: injectable conductive hydrogel; PEDOT:PSS: poly(3,4-ethylenedioxythiophene)-poly(styrenesulfonate); PSS: poly(styrenesulfonate).

glycerol forms sulfonic ester (S-O-S) bond[80]. This was further observed in the sharper S-phenyl peak[78] at 1,040 $cm^{-1}$ due to PSS stretching in the presence of glycerol [Figure 2C]. Furthermore, at the microscale, homogenous interaction and gelation were confirmed by scanning electron microscopy (SEM) as precipitation and no other irreversible crosslinking occurred, while sulfur elements, only contained in PEDOT:PSS, were uniformly dispersed [Supplementary Figure 2].

The reversible ionic crosslinking between HATYR and PEDOT:PSS was qualitatively evident [Figure 2D]; even with the addition of glycerol, the crosslinking remained, and the gelation was not disturbed as G' of both ICH and HATYR/PEDOT:PSS remained similar at around 60 Pa and viscosity was almost unchanged [Supplementary Figure 3]. In addition, the bonds between HATYR and PEDOT:PSS were clearly reversibly crosslinked owing to their self-healing capability as initial G' (15 Pa) at 0.5% strain decreased to 3.5 Pa at 1,000% strain but reverted back to the original value at the final strain of 0.5% [Supplementary Figure 4][81].

Next, we tested HATYR/PEDOT:PSS with different concentrations (0.5%, 1%, 2%, and 3%) of HATYR to quantitatively and qualitatively characterize injectability. First, the mechanical modulus of each HATYR/PEDOT:PSS sample was determined. As the concentration of HATYR increased at an oscillation frequency of 1 Hz, the storage modulus increased from 65, 223, 390, and 480 Pa at HATYR concentrations of 0.5%, 1%, 2%, and 3%, respectively, indicating robust gelation with increasing tyramine and sulfone crosslinking [Supplementary Figure 5A][43].

Recently, there have been many reports on the use of organic-based conductive hydrogels in various bioelectronic applications, including epidermal electrophysiological recording[82], 3D printable and cytocompatible conductive bioink[83], and peripheral nerve interfacing[84]. However, to the best of our knowledge, there has not yet been a reported case of a biocompatible, multi-channel recording electrode array platform fabricated from purely conductive hydrogel, not to mention a demonstration of MRI compatibility from a hydrogel ECoG array.

In addition, hydrogels fabricated with commonly used photolithography techniques are incompatible with complex geometries: photolithography is a multistep process that is increasingly more expensive and delicate with finer structures[85]. Moreover, injection- or extrusion-based printing that depends on the viscoelasticity of the hydrogel has advantages in cytotoxicity and high-fidelity post-printing. Therefore, viscoelasticity was observed with increasing HATYR concentrations, and all the hydrogel samples were found to be shear thinning, which is injectable [Supplementary Figure 5B][86]. However, the optimal concentration of HATYR should be determined qualitatively for extruded hydrogel diameters of less than 200 μm for higher-resolution patterning in array designs. A limitation of fabricating conductive hydrogel electrode arrays through extrusion is the dependence of dimensions on the size of the injection needle. Commercially available needles vary from 18 to 30 G (inner diameter of 0.838 to 0.159 μm); thus, using injection to design array design comes at the cost of large width. Therefore, we tested the injectability of each HATYR/PEDOT:PSS formulation using a 30 G needle, the thinnest inner diameter available to us. The tyramine moieties allowed for a stronger ionic crosslinking with PSS than with the HA backbone, thereby increasing the overall viscoelasticity of the formulation and injectable using a 30 G needle. Although 0.5% HATYR/PEDOT:PSS showed the formation of continuous filaments, 1% HATYR/PEDOT:PSS extruded with slight fluctuations, 2% HATYR/PEDOT:PSS was injected with granular and brittle textures, and 3% HATYR/PEDOT:PSS could not be extruded with a 30 G needle [Supplementary Figure 5C]. Therefore, a HATYR concentration of 0.5% was chosen for all subsequent experiments.

Previous FT-IR spectra analysis showed that C=O stretching at 1,736 $cm^{-1}$ of the HA backbone, although weak, also participates in crosslinking. To investigate this mechanically, an equal concentration (0.5%) of pristine HA was compared to that of HATYR when mixed with the PEDOT:PSS solution. At an oscillation frequency of 1 Hz, the storage modulus decreased by more than 4-fold from 65 to 14 Pa when tyramine was absent in the backbone [Figure 2E]. In addition, the viscoelasticity decreased, thereby losing linear injectability due to absence of tyramine moieties [Figure 2F].

A recurring problem with hydrogel bioelectronics is that hydrogels are intrinsically hydrophilic and can be easily dissolved when interfaced with wet surfaces. Therefore, ICH was prepared by adding glycerol to HATYR/PEDOT:PSS hydrogel to improve its resistance to dissolution. Firstly, the addition of glycerol did not hinder injectability and was found to be printable [Figure 2G]. Feasibility in 3D extrusion printing demonstrates the scalable and repeatable fabrication process of the electrode array for potential mechanization and precision healthcare. While molding may also be a consideration, it does not provide flexibility in design nor in the manufacturing process; thus, 3D printing was demonstrated for feasibility in

printing electrodes. Secondly, ICH was not only able to withstand complete dissolution for a longer duration in aqueous conditions but also showed high confidence in conductivity [Supplementary Figure 6A and Figure 2H]. In addition, the normalized resistivity values ($\Delta\rho/\rho_0$) and conductivity values ($\Delta\sigma/\sigma_0$) of ICH, while soaked in a PBS buffer from 0 to 16 h, showed that the conductivity of ICH was increased until 2 h ($\Delta\sigma/\sigma_0 = 2.248 \pm 0.062$), decreased via dissociation from 2 to 8 h, and dissociated completely after 16 h [Supplementary Figure 6B]. Third, cyclic strain-resistance tests were conducted to evaluate improvements in conductivity after the addition of glycerol, which improved from 6,092 Ω ($1.45 \times 10^{-2}$ S/cm) to 4,932 Ω ($1.79 \times 10^{-2}$ S/cm), and the relative normalized resistance values ($\Delta R/R_0$) after glycerol addition exhibited negligible changes of about 0.92 after 100 times cyclic strains [Figure 2I, Supplementary Figure 6C and Supplementary Figure 7]. Lastly, we assessed the feasibility of ICH in terms of electrophysiology (EMG and ECG). We first proceeded with the measurement of EMG signals using ICH to confirm the feasibility of the electrode for the recording of electrophysiological signals. In correspondence with the soft-hand gestures of the volunteer, the SNR of the enveloped EMG data was 3.87[Figure 2J]. Furthermore, the ECG signal measurement showed clear P-Q-R-S-T wave peaks, which are the typical shapes of ECG signal, confirming the feasibility of ICH as a recording electrode [Figure 2K].

### Fabrication and physicochemical evaluation of ICH-based soft and stretchable ECoG arrays

After establishing the feasibility of ICH as an electrode for implantable array devices, we proceeded with the device fabrication. Through the stable injection property of ICH, soft and stretchable 4-channel ECoG array fabrication was performed by simply extruding ICH along the 100 μm-thick molded PVDF-HFP substrate, and the channels were purposely left open for the *in situ* injection of ICH for interface with the brain tissue [Figure 3A]. Finally, the patterned soft and stretchable ECoG arrays were connected to a printed circuit board (PCB) for an implant-ready 4-channel ECoG device [Figure 3B].

The completed 4-channel array device was first optimized in UTM to evaluate the PVDF-HFP substrate for a soft and stretchable ECoG interface [Figure 3C]. The PVDF-HFP film with ICH (e.g., soft and stretchable brain interface) endured an appropriate tensile strain of more than 400% with similar toughness (576.83 kJ/m$^3$) compared to the pristine PVDF-HFP film (471.05 kJ/m$^3$). Specifically, Young's modulus of PVDF-HFP shows a minimum value of around 0.2 MPa, which is ideal for tissue mechanical modulus matching[87,88]. Therefore, these results indicate that PVDF-HFP is the most efficient substrate for brain interfaces compared to the other widely applied current elastomeric substrates (e.g., PDMS and SEBS)[89]. Satisfying the aforementioned standards, PVDF-HFP was chosen as an appropriate substrate for a soft and stretchable ECoG interface [Figure 3D].

The conformability of the soft and stretchable ECoG arrays due to the substrate deformation markedly improved the contact area between the ICH electrode and the brain phantom model [Figure 3E]. Crucially, impedance measurements at a varying range of frequencies in the PBS solution predicted the efficiency of monitoring electrophysiological signals similar to those generated by living tissues [Figure 3F][90]. Unlike purely electrical conductivity from metallic components, conductive hydrogels contain both ionic and electrical conductivity[39], which results in a low impedance value of approximately $10^0$ kΩ even in low frequencies under 1 Hz[91]. Our ICH showed similarly low impedance values (~$6 \times 10^0$ kΩ at $10^0$ Hz) and a phase angle close to 0° (maximum -10° from long connection wire and -6° from short connection wire) across all frequency ranges between $10^0$ and $10^5$ Hz[91]. These results highlight the highly stable electrophysiological performance of the hydrogel arrays for ECoG monitoring [Figure 3F and Supplementary Figure 8].

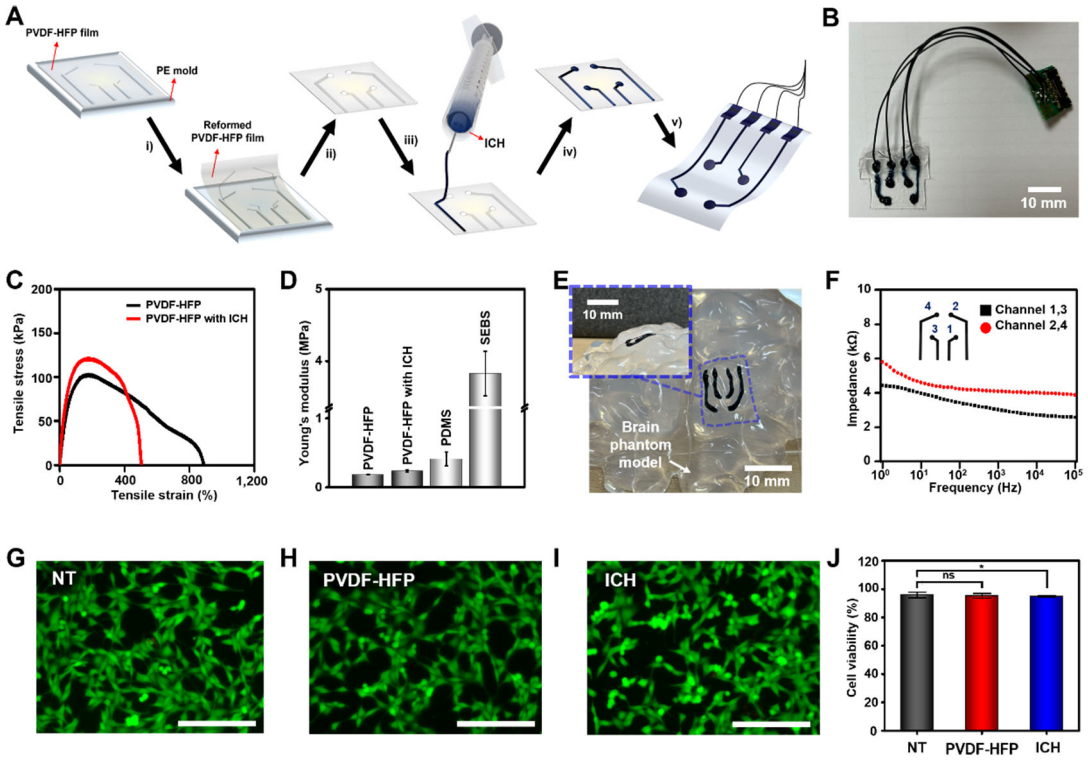


**Figure 3.** Evaluation of ICH-based soft brain interface. (A) Fabrication scheme of ICH-based soft brain interface. Each step represents: (i) reforming PVDF-HFP film, (ii) punching channel site, (iii, iv) extrusion-based printing of ICH, and (v) connecting wires to ICH arrays; (B) Photograph of ICH-based soft brain interface; (C) Evaluating tensile stress per strain of "with" or "without" ICH-injected on the PVDF-HFP; (D) Young's modulus of "with" or "without" ICH-injected PVDF-HFP and previous reported Young's modulus of "PDMS" and "SEBS"; (E) Photograph of conformal contact between ICH-based soft brain interface with brain phantom model; (F) Electrochemical impedance property of different pair of channels (long connection wire from channel "1, 3" and short connection wire from channel "2, 4") from ICH-based soft brain interface in PBS solution; (G-I) representative live/dead staining images of HT22 cells of NT (G), PVDF-HFP (H), and ICH (I) after 24 h incubation at 37°C. Living cells appear green, dead cells appear red (scale bar = 400 μm). (J) Cell viability of NT, PVDF-HFP, and ICH ($n$ = 3, mean ± SD) (*$P$ < 0.05, ns = not significant). ICH: injectable conductive hydrogel; NT: not treated; PDMS: polydimethylsiloxane; PVDF-HFP: poly(vinylidene fluoride-co-hexafluoropropylene); SEBS: styrene-ethylene/butylene-styrene.

To demonstrate the absence of cytotoxicity and biocompatibility of ICH and PVDF-HFP in the brain, HT22 mouse hippocampal neuronal cells were cultured and tested using a direct method. After 24 h of subculture, 2 $cm^2$ of PVDF-HFP film and 100 μL of ICH were placed above the monolayer of HT22 cells, each in their respective wells and supplemented with fresh media. After 24 h of incubation, the cells were treated with calcein AM to stain live cells and EthD-1 to stain dead cells. Evaluation using a fluorescence microscope revealed insignificant red staining in cells treated with ICH or PVDF-HFP [Figure 3G-I]. Overall, the recorded cell viabilities were 95.8% ± 1.9%, 95.2% ± 1.7%, and 94.8% ± 0.7% for NT, PVDF-HFP, and ICH, respectively [Figure 3J]. These results indicate that all samples exhibited homogenous proliferation and high cell viability.

### *In vivo* evaluation of ICH-based electrode array

To verify the neurophysiological capability of ICH, animal experiments to demonstrate brain interfacing were conducted using ICH-based soft electrode devices. For acute neural recording, the electrode pattern was fabricated *in situ* by printing ICH on a PVDF-HFP substrate using a syringe. The 4-channel ICH electrode device was mounted on both hemispheres of the cortex of the anesthetized animals.

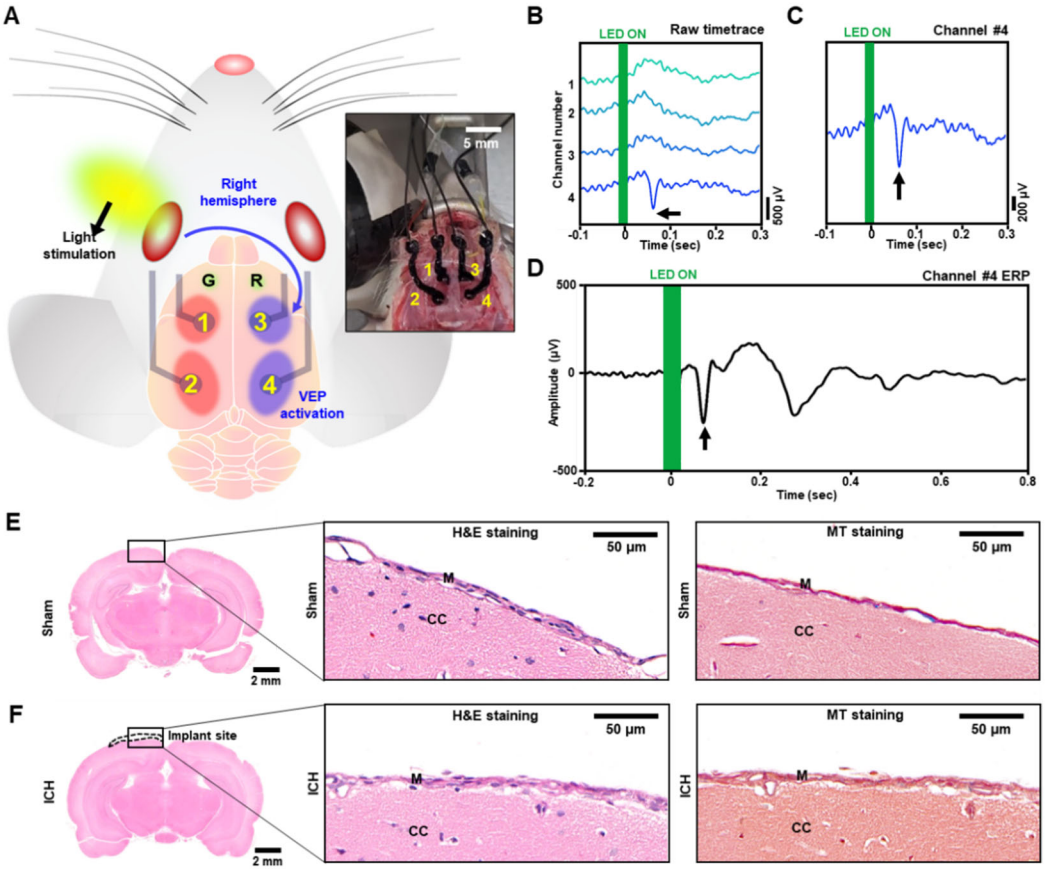


**Figure 4.** Acute ECoG recording and histological analysis. (A) Scheme of rodent VEP activation test (photograph of ICH-based ECoG array on rodent cerebral cortex, inset photo); (B) Representative baseline ECoG and VEP signals recorded by 4-channel ICH electrodes; (C) A representative VEP recorded from a channel number 4 located close to the right occipital lobe; (D) Mean VEP plot recorded by a channel number 4. Multiple VEP activation results were accumulated from 120 trials of light stimuli; (E-F) H&E staining (middle) and MT staining (right) of rodent at 4 weeks of sham (E) and after ICH implantation (F). (E, left) Representative sham rodent brain slide. (F, left) Representative ICH-implanted rodent brain slice with pseudo implant site (dotted). M: meninges; CC: cerebral cortex. ECoG: electrocorticogram; ICH: injectable conductive hydrogel; VEP: visual-related event potential.

For each hemisphere, one channel was connected to the visual cortex, and the other was located far away from the visual cortex to demonstrate the multi-channel selectivity of the ICH device. Then, the baseline ECoG signals and event-related potentials (ERPs) from the visual cortex visual-related event potential (VEP) generated following light stimulation of the left eye were recorded [Figure 4A]. As expected, the brain-like soft moduli and high ionic conductivity of the ICH enabled excellent conformal interfacing with the cortex, featuring a stable neural recording capability over the acute neural recording period. The raw plot of the baseline ECoG signal [Figure 4B] and activated VEP [Figure 4C] recorded from the 4-channel device verified the feasibility of the multi-channel configuration of ICH-based bioelectronics. Using multiple VEP activation tests, the repetitive recording capability of the ICH device for neural responses to extracorporeal stimulation was clearly demonstrated [Figure 4D]. While only acute neural recording experiments, including baseline and ERP, were demonstrated in this study, these results consistently highlight the feasibility of our ICH gel for use as printable soft brain interfaces. The elastomeric polymer we used as a substrate layer features self-healing properties, which form chemical re-bonding. A passivation layer of self-healing polymer can be easily assembled physically and chemically with the backbone substrate by autonomous self-bonding. Additionally, the hydrophobic self-healing substrate and passivation used in

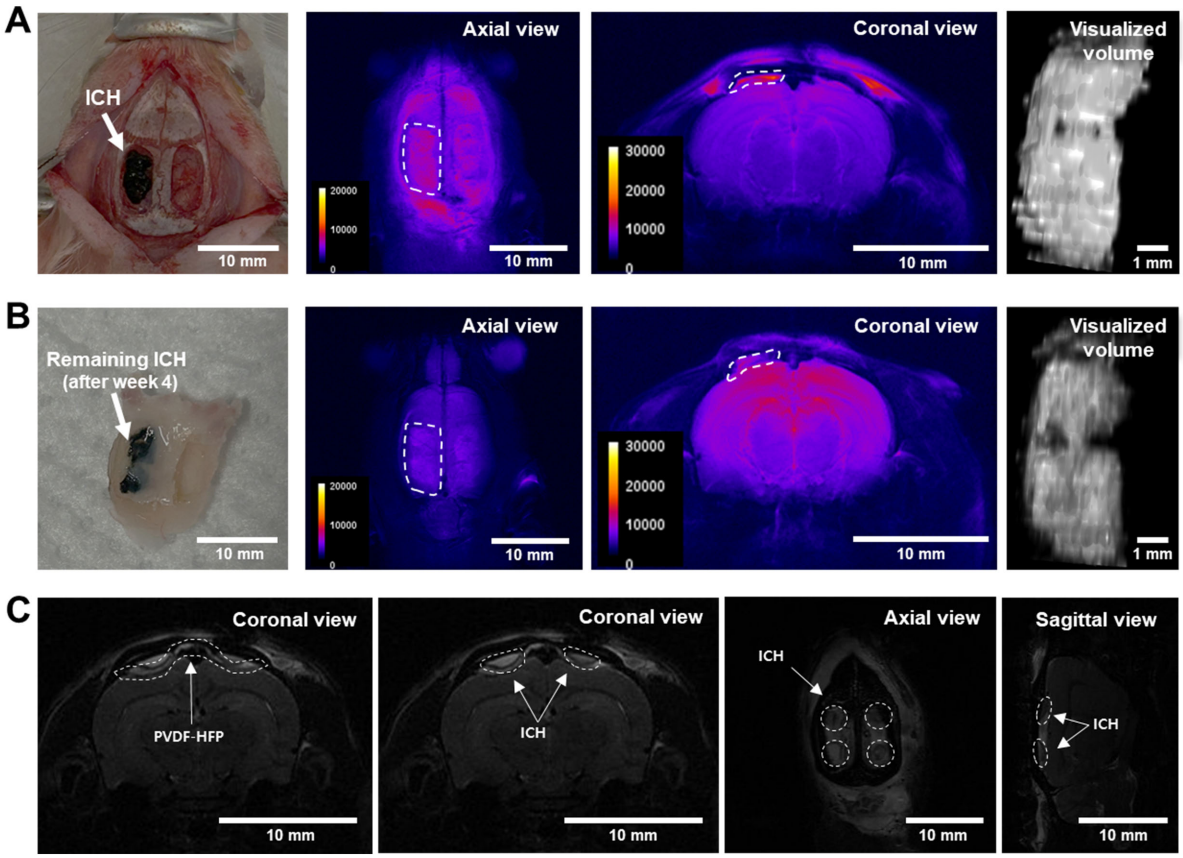


**Figure 5.** MRI of ICH and ICH-based device. (A, from left to right) Photograph of ICH at the time of implantation, axial and coronal view of the ICH subsequently after implantation, and visualized ICH volume; (B, from left to right) Photograph, axial and coronal view, and visualized ICH volume at 4 weeks after implantation; (C, from left to right) PVDF-HFP (dotted) conformally intact to brain tissue and ICH (dotted) visible without artifact in coronal, axial, and sagittal views as an electrode array device. MRI: magnetic resonance imaging; ICH: injectable conductive hydrogel; PVDF-HFP: poly(vinylidene fluoride-co-hexafluoropropylene).

this study possess water-repellent properties, which may contribute to preventing the swelling of the organic electronic device due to biofluids. Based on merits of the self-healing polymer, we expect improvements to be made in ICH-based neural devices, as well as the use of our soft, biocompatible, printable brain interface platform in chronic implants in the future. To histologically investigate the biocompatibility of ICH, H&E and MT staining was used to evaluate cellular inflammation, necrosis, apoptosis, and fibrosis. Compared to the Sham, which was subjected to the same surgical procedure, ICH implants showed little or no signs of cellular death and fibrosis, confirming the biocompatibility of our ICH [Figure 4E and F].

### Biodegradation and conformality evaluation using MRI

One of the main advantages of hydrogel-based electrode devices is their ability to degrade safely *in vivo*. The biodegradation of implanted devices after recording physiological signals removes the need to undergo additional surgery to remove the device, thus enhancing patient survival.

The magnetic resonance technique is widely used in non-invasive *in vivo* studies because of its ability to image without damaging tissues or samples. Therefore, we utilized MRI to image the *in vivo* biodegradation of ICH over a period of four weeks to demonstrate the stable and conformal attachment of the electrode array device after implantation surgery.

Although PEDOT:PSS is not biodegradable and is reported to circulate through the renal system to be cleared from the body[92], it has been used in many neural engineering applications due to its low immunogenicity[93,94]. Conversely, the main route of biodegradation of ICH is postulated to be achieved via its enzymatic degradation from hyaluronidase and by increased hydrolysis at the hydrophilic domains of HA[95,96]. Thus, to evaluate its biodegradation, ICH was imaged initially after the 1-mL injection of ICH over the left hemisphere of the cerebral cortex. After calibrating the brightness and contrast relative to 0 week as the baseline, the minimum and maximum brightness values were set to 0 and 30,000, respectively [Figure 5A]. After 4 weeks, the same rodent was imaged and analyzed using calibrated brightness and contrast, and approximately 0.4 mL of the injected volume was found to remain [Figure 5B]. These results demonstrate that ICH is safely biodegraded, further confirming the feasibility of ICH as a controllable degrading electrode array.

Next, rodents implanted with an electrode array device were imaged three days after surgery. In the coronal view, ICH and PVDF-HFP were clearly visible individually without the disturbance of resonance, which is unavoidable when using metal-based electrodes[33], and showed conformal contact. In the axial and sagittal views, the ICH channels were also evident and did not inundate outside of the channel [Figure 5C].

## CONCLUSIONS

In this study, an unconventional injectable bioelectronic material composed of purely organic polymers was developed to implement as a MRI-compatible brain-interfacing device. The ICH has numerous advantages that are essential for implantable bioelectronics. First, ICH is injectable *in situ* into a high-resolution (less than 200 μm diameter) linear array pattern due to the ionically crosslinked (hydrogen bonding between tyramine and sulfone) hydrogel. Second, it is highly biocompatible both *in vitro* (95.9% cell viability) and *in vivo* (no signs of inflammation and fibrosis), along with a rate of degradation of up to 40% of its original volume within four weeks. Third, brain conformal, soft neural electrodes for ECoG recording are demonstrated using a rodent model with a clear VEP signal from the visual cortex. Finally, no artifacts were generated by the device on MRI, as ICH and PVDF-HFP were clearly imaged without resonance distortion. As a result, based on its brain-like soft moduli and excellent ionic conductivity, MRI-compatible ICH neural electrodes realized stable ECoG monitoring with highly sensitive documentation of neural responses to visual stimulation, which could be further expanded to recording other neural responses from various senses, such as olfactory, tactile, and auditory senses, using our ICH-based brain-interfacing platform.

## DECLARATIONS

### Acknowledgments

We thank Chanhee Lee and the Center for Neuroscience Imaging Research for the imaging of 9.4T animal MRI. We would also like to thank Jin-Hwan Jeon of the Center for Neuroscience Imaging Research for the 3D printing of the substrate mold.

### Authors' contributions

Substantial contributions to the conception and design of the study and performed data analysis and interpretation: Kim SD, Park K, Lee S

Data acquisition and administrative, technical, and material support: Kim SD, Park K, Lee S, Kum J, Ahn S, Kim Y, Kim J

Review, editing, and supervision of this project: Shin M, Son D

Kim SD, Park K, and Lee S contributed equally to the article.

### Availability of data and materials

The authors confirm that the data supporting the findings of this study are available in the article and its supplementary material.

### Financial support and sponsorship

This research was supported by the Institute for Basic Science (IBS-R015-D1), by a National Research Foundation of Korea (NRF) grant funded by the Korean government (MSIT) (Nos. 2020R1C1C1005567 and 2022M3E5E9018583), and by the Korean Fund for Regenerative Medicine (KFRM) grant funded by the Korea government (the Ministry of Science and ICT, the Ministry of Health & Welfare) (code: 23B0102L1)

### Conflicts of interest

All authors declare that there are no conflicts of interest.

### Ethical approval and consent to participate

The animal experiments for ECoG monitoring were conducted by obtaining Institutional Animal Care and Use Committee (IACUC) approval (KIST-2021-12-159) from the Korea Institute of Science and Technology. The authors also obtained Institutional Review Board (IRB) approval (No. SKKU 2022-08-020) from Sungkyunkwan University for real-time measurement of the ECG and EMG signals.

### Consent for publication

Not applicable.



## REFERENCES

1. Kim DH, Ahn JH, Choi WM, et al. Stretchable and foldable silicon integrated circuits. *Science* 2008;320:507-11. DOI
2. Cho KW, Sunwoo SH, Hong YJ, et al. Soft bioelectronics based on nanomaterials. *Chem Rev* 2022;122:5068-143. DOI
3. Boutry CM, Negre M, Jorda M, et al. A hierarchically patterned, bioinspired e-skin able to detect the direction of applied pressure for robotics. *Sci Robot* 2018;3:eaau6914. DOI
4. Liu Y, Norton JJ, Qazi R, et al. Epidermal mechano-acoustic sensing electronics for cardiovascular diagnostics and human-machine interfaces. *Sci Adv* 2016;2:e1601185. DOI PubMed PMC
5. Chun KS, Kang YJ, Lee JY, et al. A skin-conformable wireless sensor to objectively quantify symptoms of pruritus. *Sci Adv* 2021:7. DOI PubMed PMC
6. Kim J, Lee M, Shim HJ, et al. Stretchable silicon nanoribbon electronics for skin prosthesis. *Nat Commun* 2014;5:5747. DOI
7. Kim SH, Baek GW, Yoon J, et al. A bioinspired stretchable sensory-neuromorphic system. *Adv Mater* 2021;33:e2104690. DOI PubMed
8. Seo H, Han SI, Song KI, et al. Durable and fatigue-resistant soft peripheral neuroprosthetics for in vivo bidirectional signaling. *Adv Mater* 2021;33:e2007346. DOI PubMed
9. Lim S, Son D, Kim J, et al. Transparent and stretchable interactive human machine interface based on patterned graphene heterostructures. *Adv Funct Mater* 2015;25:375-83. DOI
10. Jung YH, Yoo J, Vázquez-guardado A, et al. A wireless haptic interface for programmable patterns of touch across large areas of the skin. *Nat Electron* 2022;5:374-85. DOI
11. Song KI, Seo H, Seong D, et al. Adaptive self-healing electronic epineurium for chronic bidirectional neural interfaces. *Nat Commun* 2020;11:4195. DOI PubMed PMC
12. Choi S, Han SI, Jung D, et al. Highly conductive, stretchable and biocompatible Ag-Au core-sheath nanowire composite for wearable and implantable bioelectronics. *Nat Nanotechnol* 2018;13:1048-56. DOI PubMed
13. Minev IR, Musienko P, Hirsch A, et al. Biomaterials. Electronic dura mater for long-term multimodal neural interfaces. *Science* 2015;347:159-63. DOI
14. Kim DH, Viventi J, Amsden JJ, et al. Dissolvable films of silk fibroin for ultrathin conformal bio-integrated electronics. *Nat Mater* 2010;9:511-7. DOI PubMed PMC
15. Tian L, Zimmerman B, Akhtar A, et al. Large-area MRI-compatible epidermal electronic interfaces for prosthetic control and cognitive monitoring. *Nat Biomed Eng* 2019;3:194-205. DOI

16. Rathi S, Deckert M, Brinkhues S, et al. PEDOT:PSS as a transparent electrically conducting polymer for brain stimulation electrodes. In: 2019 IEEE 16th India Council International Conference (INDICON).2019. p. 1-4. DOI
17. Wang Y, Zhu C, Pfattner R, et al. A highly stretchable, transparent, and conductive polymer. *Sci Adv* 2017;3:e1602076. DOI PubMed PMC
18. Lu B, Yuk H, Lin S, et al. Pure PEDOT:PSS hydrogels. *Nat Commun* 2019;10:1043. DOI PubMed PMC
19. Feig VR, Tran H, Lee M, Bao Z. Mechanically tunable conductive interpenetrating network hydrogels that mimic the elastic moduli of biological tissue. *Nat Commun* 2018;9:2740. DOI PubMed PMC
20. Feig VR, Tran H, Lee M, et al. An electrochemical gelation method for patterning conductive PEDOT:PSS hydrogels. *Adv Mater* 2019;31:e1902869. DOI
21. Palumbiny CM, Liu F, Russell TP, Hexemer A, Wang C, Müller-Buschbaum P. The crystallization of PEDOT:PSS polymeric electrodes probed in situ during printing. *Adv Mater* 2015;27:3391-7. DOI PubMed
22. Jiang Y, Zhang Z, Wang YX, et al. Topological supramolecular network enabled high-conductivity, stretchable organic bioelectronics. *Science* 2022;375:1411-7. DOI
23. Green R. Elastic and conductive hydrogel electrodes. *Nat Biomed Eng* 2019;3:9-10. DOI PubMed
24. Jo YJ, Kim SY, Hyun JH, et al. Fibrillary gelation and dedoping of PEDOT:PSS fibers for interdigitated organic electrochemical transistors and circuits. *npj Flex Electron* 2022:6. DOI
25. Lu L, Fu X, Liew Y, et al. Soft and MRI compatible neural electrodes from carbon nanotube fibers. *Nano Lett* 2019;19:1577-86. DOI
26. Chen G, Dodson B, Johnson F, et al. Tissue-susceptibility matched carbon nanotube electrodes for magnetic resonance imaging. *J Magn Reson* 2018;295:72-9. DOI
27. Ye F, Li M, Ke D, Wang L, Lu Y. Ultrafast Self□healing and injectable conductive hydrogel for strain and pressure sensors. *Adv Mater Technol* 2019;4:1900346. DOI
28. Tringides CM, Vachicouras N, de Lázaro I, et al. Viscoelastic surface electrode arrays to interface with viscoelastic tissues. *Nat Nanotechnol* 2021;16:1019-29. DOI PubMed PMC
29. Son D, Kang J, Vardoulis O, et al. An integrated self-healable electronic skin system fabricated via dynamic reconstruction of a nanostructured conducting network. *Nat Nanotechnol* 2018;13:1057-65. DOI
30. Zhao S, Liu X, Xu Z, et al. Graphene encapsulated copper microwires as highly MRI compatible neural electrodes. *Nano Lett* 2016;16:7731-8. DOI
31. Bakhshaee Babaroud N, Palmar M, Velea AI, et al. Multilayer CVD graphene electrodes using a transfer-free process for the next generation of optically transparent and MRI-compatible neural interfaces. *Microsyst Nanoeng* 2022;8:107. DOI PubMed PMC
32. Oribe S, Yoshida S, Kusama S, et al. Hydrogel-based organic subdural electrode with high conformability to brain surface. *Sci Rep* 2019;9:13379. DOI PubMed PMC
33. Fallegger F, Schiavone G, Pirondini E, et al. MRI-compatible and conformal electrocorticography grids for translational research. *Adv Sci* 2021;8:2003761. DOI PubMed PMC
34. Chen R, Canales A, Anikeeva P. Neural recording and modulation technologies. *Nat Rev Mater* 2017;2:16093. DOI PubMed PMC
35. Kim DH, Lu N, Ma R, et al. Epidermal electronics. *Science* 2011;333:838-43. DOI
36. Kim N, Kim J, Seo J, Hong C, Lee J. Stretchable inorganic LED displays with double-layer modular design for high fill factor. *ACS Appl Mater Interfaces* 2022;14:4344-51. DOI
37. Jang KI, Chung HU, Xu S, et al. Soft network composite materials with deterministic and bio-inspired designs. *Nat Commun* 2015;6:6566. DOI PubMed PMC
38. Liu J, Zhang X, Liu Y, et al. Intrinsically stretchable electrode array enabled in vivo electrophysiological mapping of atrial fibrillation at cellular resolution. *Proc Natl Acad Sci U S A* 2020;117:14769-78. DOI PubMed PMC
39. Yuk H, Lu B, Zhao X. Hydrogel bioelectronics. *Chem Soc Rev* 2019;48:1642-67. DOI PubMed
40. Lee YY, Kang HY, Gwon SH, et al. A Strain-insensitive stretchable electronic conductor: PEDOT:PSS/acrylamide organogels. *Adv Mater* 2016;28:1636-43. DOI
41. Yang Q, Wei T, Yin RT, et al. Photocurable bioresorbable adhesives as functional interfaces between flexible bioelectronic devices and soft biological tissues. *Nat Mater* 2021;20:1559-70. DOI PubMed PMC
42. Son D, Lee J, Qiao S, et al. Multifunctional wearable devices for diagnosis and therapy of movement disorders. *Nat Nanotechnol* 2014;9:397-404. DOI
43. Ju J, Kim J, Choi Y, et al. Punicalagin-loaded alginate/chitosan-gallol hydrogels for efficient wound repair and hemostasis. *Polymers* 2022;14:3248. DOI PubMed PMC
44. Kim J, Ju J, Kim SD, Shin M. Plant-inspired Pluronic-gallol micelles with low critical micelle concentration, high colloidal stability, and protein affinity. *Biomater Sci* 2022;10:3739-46. DOI PubMed
45. Shin M, Song KH, Burrell JC, Cullen DK, Burdick JA. Injectable and conductive granular hydrogels for 3D printing and electroactive tissue support. *Adv Sci* 2019;6:1901229. DOI PubMed PMC
46. Uman S, Dhand A, Burdick JA. Recent advances in shear□thinning and self-healing hydrogels for biomedical applications. *J Appl Polym Sci* 2020;137:48668. DOI
47. Jin S, Kim Y, Son D, Shin M. Tissue adhesive, conductive, and injectable cellulose hydrogel ink for on-skin direct writing of electronics. *Gels* 2022;8:336. DOI PubMed PMC
48. Shin M, Park E, Lee H. Plant-inspired pyrogallol-containing functional materials. *Adv Funct Mater* 2019;29:1903022. DOI

49. Kim S, Choi H, Son D, Shin M. Conductive and adhesive granular alginate hydrogels for on-tissue writable bioelectronics. *Gels* 2023;9:167. DOI PubMed PMC
50. Lee KY, Mooney DJ. Hydrogels for tissue engineering. *Chem Rev* 2001;101:1869-79. DOI PubMed
51. Dromel PC, Singh D, Andres E, et al. A bioinspired gelatin-hyaluronic acid-based hybrid interpenetrating network for the enhancement of retinal ganglion cells replacement therapy. *NPJ Regen Med* 2021;6:85. DOI PubMed PMC
52. Xing F, Zhou C, Hui D, et al. Hyaluronic acid as a bioactive component for bone tissue regeneration: Fabrication, modification, properties, and biological functions. *Nanotechno Rev* 2020;9:1059-79. DOI
53. Kim S, Shin M. Role of free catecholamine in thiol-ene crosslinking for hyaluronic acid hydrogels with high loading efficiency of anticancer drugs. *Tissue Eng Regen Med* 2022;19:281-7. DOI PubMed PMC
54. Shin J, Choi S, Kim JH, et al. Tissue adhesives: tissue tapes-phenolic hyaluronic acid hydrogel patches for off-the-shelf therapy (Adv. Funct. Mater. 49/2019). *Adv Funct Mater* 2019;29:1970331. DOI
55. Choi S, Lee JS, Shin J, et al. Osteoconductive hybrid hyaluronic acid hydrogel patch for effective bone formation. *J Control Release* 2020;327:571-83. DOI
56. An S, Choi S, Min S, Cho S. Hyaluronic acid-based biomimetic hydrogels for tissue engineering and medical applications. *Biotechnol Bioproc E* 2021;26:503-16. DOI
57. Kim KS, Park SJ, Yang JA, et al. Injectable hyaluronic acid-tyramine hydrogels for the treatment of rheumatoid arthritis. *Acta Biomater* 2011;7:666-74. DOI PubMed
58. Kurisawa M, Chung JE, Yang YY, Gao SJ, Uyama H. Injectable biodegradable hydrogels composed of hyaluronic acid-tyramine conjugates for drug delivery and tissue engineering. *Chem Commun* 2005:4312-4. DOI PubMed
59. Kim SD, Jin S, Kim S, Son D, Shin M. Tyramine-functionalized alginate-collagen hybrid hydrogel inks for 3D-bioprinting. *Polymers* 2022;14:3173. DOI PubMed PMC
60. Lee F, Chung JE, Kurisawa M. An injectable hyaluronic acid-tyramine hydrogel system for protein delivery. *J Control Release* 2009;134:186-93. DOI PubMed
61. Wang LS, Lee F, Lim J, et al. Enzymatic conjugation of a bioactive peptide into an injectable hyaluronic acid-tyramine hydrogel system to promote the formation of functional vasculature. *Acta Biomater* 2014;10:2539-50. DOI PubMed
62. Lee F, Chung JE, Kurisawa M. An injectable enzymatically crosslinked hyaluronic acid- hydrogel system with independent tuning of mechanical strength and gelation rate. *Soft Matter* 2008;4:880-7. DOI PubMed
63. Shin J, Choi EJ, Cho JH, et al. Three-dimensional electroconductive hyaluronic acid hydrogels incorporated with carbon nanotubes and polypyrrole by catechol-mediated dispersion enhance neurogenesis of human neural stem cells. *Biomacromolecules* 2017;18:3060-72. DOI
64. Kim S, Jang Y, Jang LK, et al. Electrochemical deposition of dopamine-hyaluronic acid conjugates for anti-biofouling bioelectrodes. *J Mater Chem B* 2017;5:4507-13. DOI PubMed
65. Kim J, Kim S, Son D, Shin M. Phenol-hyaluronic acid conjugates: correlation of oxidative crosslinking pathway and adhesiveness. *Polymers* 2021;13:3130. DOI PubMed PMC
66. Kim SH, Kim Y, Choi H, et al. Mechanically and electrically durable, stretchable electronic textiles for robust wearable electronics. *RSC Adv* 2021;11:22327-33. DOI PubMed PMC
67. Song J, Kim Y, Kang K, Lee S, Shin M, Son D. Stretchable and Self-healable graphene-polymer conductive composite for wearable EMG sensor. *Polymers* 2022;14:3766. DOI PubMed PMC
68. Park K, Kang K, Kim J, et al. Balanced coexistence of reversible and irreversible covalent bonds in a conductive triple polymeric network enables stretchable hydrogels with high toughness and adhesiveness. *ACS Appl Mater Interfaces* 2022;14:56395-406. DOI
69. Lee S, Park K, Kum J, et al. Stretchable surface electrode arrays using an alginate/PEDOT:PSS-based conductive hydrogel for conformal brain interfacing. *Polymers* 2022;15:84. DOI PubMed PMC
70. Park K, Choi H, Kang K, Shin M, Son D. Soft stretchable conductive carboxymethylcellulose hydrogels for wearable sensors. *Gels* 2022;8:92. DOI PubMed PMC
71. Kim Y, Song J, An S, Shin M, Son D. Soft liquid metal-based conducting composite with robust electrical durability for a wearable electrocardiogram sensor. *Polymers* 2022;14:3409. DOI PubMed PMC
72. Sun JY, Zhao X, Illeperuma WR, et al. Highly stretchable and tough hydrogels. *Nature* 2012;489:133-6. DOI PubMed PMC
73. Ju J, Jin S, Kim S, et al. Addressing the shortcomings of polyphenol-derived adhesives: achievement of long shelf life for effective hemostasis. *ACS Appl Mater Interfaces* 2022;14:25115-25. DOI
74. Oliva N, Shin M, Burdick JA. Editorial: special issue on advanced biomedical hydrogels. *ACS Biomater Sci Eng* 2021;7:3993-6. DOI PubMed
75. Choi Y, Kang K, Son D, Shin M. Molecular rationale for the design of instantaneous, strain-tolerant polymeric adhesive in a stretchable underwater human-machine interface. *ACS Nano* 2022;16:1368-80. DOI PubMed
76. Nguyen LTB, Hsu CC, Ye H, Cui Z. Development of an in situ injectable hydrogel containing hyaluronic acid for neural regeneration. *Biomed Mater* 2020;15:055005. DOI
77. Moraes MR, Alves AC, Toptan F, et al. Glycerol/PEDOT:PSS coated woven fabric as a flexible heating element on textiles. *J Mater Chem C* 2017;5:3807-22. DOI
78. Koizumi Y, Ohira M, Watanabe T, Nishiyama H, Tomita I, Inagi S. Synthesis of poly(3,4-ethylenedioxythiophene)-platinum and poly(3,4-ethylenedioxythiophene)-poly(styrenesulfonate) hybrid fibers by alternating current bipolar electropolymerization. *Langmuir*

2018;34:7598-603. DOI PubMed

79. Liu X, Zai J, Iqbal A, et al. Glycerol-crosslinked PEDOT:PSS as bifunctional binder for Si anodes: Improved interfacial compatibility and conductivity. *J Colloid Interface Sci* 2020;565:270-7. DOI
80. Kim J, Jang JG, Kwak J, Hong JI, Kim SH. Enhanced humid reliability of organic thermoelectrics via crosslinking with glycerol. *Nanomaterials* 2019;9:1591. DOI PubMed PMC
81. Choi Y, Park K, Choi H, Son D, Shin M. Self-healing, stretchable, biocompatible, and conductive alginate hydrogels through dynamic covalent bonds for implantable electronics. *Polymers* 2021;13:1133. DOI PubMed PMC
82. Wang Z, Chen L, Chen Y, Liu P, Duan H, Cheng P. 3D printed ultrastretchable, hyper-antifreezing conductive hydrogel for sensitive motion and electrophysiological signal monitoring. *Research* 2020;2020:1426078. DOI PubMed PMC
83. Aggas JR, Abasi S, Phipps JF, Podstawczyk DA, Guiseppi-Elie A. Microfabricated and 3-D printed electroconductive hydrogels of PEDOT:PSS and their application in bioelectronics. *Biosens Bioelectron* 2020;168:112568. DOI PubMed
84. Hiendlmeier L, Zurita F, Vogel J, et al. 4D-Printed soft and stretchable self-folding cuff electrodes for small-nerve interfacing. *Adv Mater* 2023;35:e2210206. DOI PubMed
85. Puza F, Lienkamp K. 3D printing of polymer hydrogels-from basic techniques to programmable actuation. *Adv Funct Materials* 2022;32:2205345. DOI
86. Kim K, Choi JH, Shin M. Mechanical stabilization of alginate hydrogel fiber and 3D constructs by mussel-inspired catechol modification. *Polymers* 2021;13:892. DOI PubMed PMC
87. Jeong JW, Shin G, Park SI, Yu KJ, Xu L, Rogers JA. Soft materials in neuroengineering for hard problems in neuroscience. *Neuron* 2015;86:175-86. DOI
88. Lacour SP, Courtine G, Guck J. Materials and technologies for soft implantable neuroprostheses. *Nat Rev Mater* 2016:1. DOI
89. Kang J, Son D, Wang GN, et al. Tough and water-insensitive self-healing elastomer for robust electronic skin. *Adv Mater* 2018;30:e1706846. DOI PubMed
90. Lim C, Hong YJ, Jung J, et al. Tissue-like skin-device interface for wearable bioelectronics by using ultrasoft, mass-permeable, and low-impedance hydrogels. *Sci Adv* 2021:7. DOI PubMed PMC
91. Liu Y, Liu J, Chen S, et al. Soft and elastic hydrogel-based microelectronics for localized low-voltage neuromodulation. *Nat Biomed Eng* 2019;3:58-68. DOI
92. Shahini A, Yazdimamaghani M, Walker KJ, et al. 3D conductive nanocomposite scaffold for bone tissue engineering. *Int J Nanomedicine* 2014;9:167-81. DOI PubMed PMC
93. Ouyang L, Shaw CL, Kuo CC, Griffin AL, Martin DC. In vivo polymerization of poly(3,4-ethylenedioxythiophene) in the living rat hippocampus does not cause a significant loss of performance in a delayed alternation task. *J Neural Eng* 2014;11:026005. DOI PubMed PMC
94. Filho G, Júnior C, Spinelli B, Damasceno I, Fiuza F, Morya E. All-polymeric electrode based on PEDOT:PSS for in vivo neural recording. *Biosensors* 2022;12:853. DOI PubMed PMC
95. Feig VR, Tran H, Bao Z. Biodegradable polymeric materials in degradable electronic devices. *ACS Cent Sci* 2018;4:337-48. DOI PubMed PMC
96. Uva A, Lin A, Babi J, Tran H. Bioderived and degradable polymers for transient electronics. *J of Chemical Tech & Biotech* 2022;97:801-9. DOI